The Astrophysical Journal, 984:51 (11pp), 2025 May 1 https://doi.org/10.3847/1538-4357/adc5f9

Methods for Tracking Cosmic-Ray Spectral Changes Using Neutron Monitors at High Cutoff Rigidity

S. Khamphakdee[1], W. Nuntiyakul[2], C. Banglieng[3], A. Seripienlert[4], P. Yakum[1], A. Sáiz[5], D. Ruffolo[5], P. Evenson[6], K. Munakata[7], and S. Komonjinda[2]
[1] Graduate Program in Astronomy, Department of Physics and Materials Science, Faculty of Science, Chiang Mai University, Chiang Mai 50200, Thailand
[2] Department of Physics and Materials Science, Faculty of Science, Chiang Mai University, Chiang Mai 50200, Thailand; waraporn.n@cmu.ac.th
[3] Division of Physics, Faculty of Science and Technology, Rajamangala University of Technology Thanyaburi, Pathum Thani 12110, Thailand
[4] Office of Research Administration, Chiang Mai University, Chiang Mai 50200, Thailand
[5] Department of Physics, Faculty of Science, Mahidol University, Bangkok 10400, Thailand
[6] Department of Physics and Astronomy, University of Delaware, Newark, DE 19716, USA
[7] Physics Department, Shinshu University, Matsumoto, Nagano 390-8621, Japan
Received 2025 January 24; revised 2025 March 13; accepted 2025 March 24; published 2025 April 25

Abstract

Neutron monitors are a standard tool for high-precision monitoring of changes in the Galactic cosmic ray (GCR) flux that occur as a result of variations of the heliospheric conditions and solar storms. In Thailand, we have developed a mobile neutron monitor named "Changvan" based on the 3NM64 design, except that the middle counter lacks lead producer rings, so we call it a semileaded neutron monitor. From 2021 April to 2023 April, the Changvan operated at the Science and Technology Park, Mae Hia, Chiang Mai, Thailand, at an altitude of about 340 m above sea level, with a vertical cutoff rigidity of 16.7 GV, which is near the highest value observed globally. With a similar cutoff rigidity, the nearby Princess Sirindhorn Neutron Monitor is an 18NM64 at the summit of Doi Inthanon, the highest mountain in Thailand, at 2560 m above sea level. We examine how count rates at different altitudes with similar cutoffs, count rates from the unleaded versus leaded counters, and the leader fraction measured from time-delay histograms all reflect GCR spectral differences, thus providing a variety of techniques for tracking cosmic-ray spectral changes. Applied at high cutoff rigidity, these methods extend the reach of the worldwide neutron monitor network to even higher rigidity.

Unified Astronomy Thesaurus concepts: Cosmic ray detectors (325); Galactic cosmic rays (567); Space weather (2037); Solar-terrestrial interactions (1473)

1. Introduction

Galactic cosmic rays (GCRs) are highly energetic particles originating from outside the solar system with spectra at Earth that are modulated by interplanetary magnetic fields influenced by solar activity (J. A. Simpson 1983). Neutron monitors are essential tools for observing variations in GCR intensity, providing valuable data to understand solar–terrestrial interactions, cosmic-ray modulation, and space weather forecasting (J. A. Simpson 2000; J. A. Lockwood et al. 2002; M. S. Potgieter 2013).

Neutron monitors are excellent at measuring changes in the overall cosmic-ray flux at a given location, sometimes achieving a statistical precision of $<0.1\%$ in hourly rates. Detecting spectral changes—variations in the relative flux as a function of energy—is harder, but good estimates over yearly timescales can be made by comparing monitors at different geomagnetic cutoffs (J. A. Simpson 2000). True precision is hard to obtain because no two monitors are identical. There are always differences in altitude, environment, and construction (P. S. Mangeard et al. 2016a; A. Mishev et al. 2021), as well as significant variations in the geomagnetic cutoff over relevant timescales (P.-S. Mangeard et al. 2018). There is also a fundamental limitation in that significant spectral modulation occurs for rigidity (defined as $P = pc/q$ for particle momentum p and charge q) above the highest available geomagnetic cutoff (C. Banglieng et al. 2020).

Such differences can be exploited to detect and even quantify spectral changes with measurements from monitors with different characteristics. Comparison of count rates from nearby monitors at different altitudes has been successfully used to study the spectral index of solar energetic particles (J. A. Lockwood et al. 2002), where the spectral index is defined as γ such that the flux has an approximate rigidity dependence as $j \propto P^{-\gamma}$. An altitude survey of the count rate of a mini neutron monitor was performed by A. Lara et al. (2016). Monitors of different constructions have also been used, such as a standard monitor and bare neutron detectors (J. W. Bieber & P. Evenson 1991; W. Nuntiyakul et al. 2018), especially to determine the spectral index of relativistic solar ions (J. W. Bieber et al. 2002, 2013; D. Ruffolo et al. 2006). Other configurations, such as the semileaded design discussed later in this paper, also have interesting properties.

Examining interactions within the monitor itself can also track spectral change. For many years, counting multiplicity has been recognized as relevant to the primary cosmic-ray energy (T. M. Aleksanyan et al. 1979; J. W. Bieber et al. 2004). Recently, more detailed measurements of interactions within the monitor have been performed. One of these, the leader fraction—the proportion of neutron detection events not associated with a preceding detection from the same cosmic ray—has been shown to be a proxy for the spectral index (P. S. Mangeard et al. 2016b; D. Ruffolo et al. 2016; C. Banglieng et al. 2020; P. Yakum et al. 2023; P. Muangha et al. 2024).

Figure 1. Photographs of the Princess Sirindhorn Neutron Monitor Station (PSNM) and the Changvan. (a) PSNM at the summit of Doi Inthanon, Thailand's highest mountain (2560 m above sea level). (b) Interior view of PSNM showing the 18-tube NM64. (c) Changvan at the Science and Technology Park, Mae Hia, Chiang Mai (340 m above sea level). (d) Semileaded (middle counter without lead producer) neutron monitor inside Changvan.

This study uses data collected between 2021 April and 2023 April from two neutron monitors (Figure 1): the Princess Sirindhorn Neutron Monitor (PSNM) at Doi Inthanon (2560 m) and the Changvan mobile neutron monitor at the Science and Technology Park, Chiang Mai (340 m). Taken together, the two neutron monitors have differences in all the key aspects discussed above. By examining neutron count rates and leader fractions under varying environmental conditions, this study enhances our understanding of GCR spectral behavior, which is crucial for improving space weather forecasting and deepening our knowledge of solar modulation effects on cosmic rays. Tracking spectral variations of cosmic rays can provide early warning signs for space weather events, as spectral shifts can indicate changes in solar activity and magnetic field configurations (A. Belov 2000; H. Mavromichalaki et al. 2011). Geomagnetic storms and other space weather phenomena affect satellite operations, communications, and power grids (K. Kudela et al. 2000). The primary goal of this study is to explore how neutron monitor data from different altitudes and configurations can be used to track spectral changes in cosmic rays, improving the precision and reliability of GCR spectral variation measurements (D. Ruffolo et al. 2016).

2. Configuration and Observations

2.1. Princess Sirindhorn Neutron Monitor

The PSNM, shown in Figure 1(a), has operated since 2007 at the summit of Doi Inthanon, Thailand's highest mountain (2560 m above sea level—18.59°N, 98.49°E). It is equipped with an 18-tube neutron monitor (18NM64), shown in Figure 1(b). Due to its strategic position at the highest vertical geomagnetic cutoff rigidity for a fixed station, 16.7 GV, PSNM plays a critical role in anchoring the high-energy end of GCRs that can be monitored with the global neutron monitor network. Its high-altitude location enhances neutron count rates, as the thinner atmosphere leads to reduced absorption of cosmic-ray showers, allowing more precise observations of cosmic rays (D. Ruffolo et al. 2016). The high rigidity cutoff makes this station invaluable for studying cosmic-ray modulation at the upper end of the energy spectrum accessible to neutron monitors.

2.2. Changvan

A summary of the main characteristics of PSNM and Changvan is provided in Table 1. The Changvan is a mobile detector developed in Thailand and housed in a standard, insulated shipping container as shown in Figure 1(c). It comprises three neutron counters as shown in Figure 1(d). Changvan has a layout similar to a 3NM64, but its middle counter lacks lead-ring producers. For brevity we refer to this counter as "unleaded," but a better term would be "semileaded" since most of the count rate comes from neutrons escaping from the adjacent fully leaded detectors. This causes a major difference in behavior compared to a standard monitor. Originally designed for conducting latitude surveys to study cosmic-ray modulation, the Changvan used Earth's magnetic field as a spectrometer to measure cosmic-ray count rates at various latitudes (K. Poopakun et al. 2023). This technique, known as the latitude survey, detects subtle changes in cosmic-ray spectra from variations in the neutron monitor counting rate as the detector traverses different geomagnetic cutoffs.

After completing the latitude survey in 2020, Changvan was operated as a fixed station from 2021 April to 2023 April at the Science and Technology Park, Mae Hia, Chiang Mai, Thailand (340 m above sea level—18.76°N, 98.94°E). (Subsequently,

Table 1
Details of Princess Sirindhorn Neutron Monitor (PSNM) and Changvan

	PSNM	Changvan
Configuration	18NM64 plus three bare counters	3NM64 design; middle counter lacks lead-ring producers (semileaded)
Location	Summit of Doi Inthanon, Thailand's highest mountain	Science and Technology Park, Mae Hia, Chiang Mai, Thailand
Elevation	2560 m above sea level	340 m above sea level
Vertical cutoff rigidity	16.69 ± 0.02 GV	16.66 ± 0.02 GV

Changvan was redeployed on a ship to perform another latitude survey.) The vertical cutoff rigidity at Mae Hia is also 16.7 GV, making it ideal for comparison with PSNM in tracking cosmic-ray spectral variations at different altitudes.

2.3. Data Accumulation

At PSNM, the average count rate per tube is approximately 34 counts s^{-1}. In contrast, the Changvan neutron monitor leaded tubes have an average count rate per tube of approximately 5.5 counts s^{-1}, with the unleaded tube having a lower count rate of approximately 3.6 counts s^{-1}. The higher count rate at PSNM is primarily due to the reduced atmospheric depth. Count rates were recorded by similar electronic systems at both locations with 10 s resolution.

In addition, the time interval between successive counts was measured with a resolution of 2.17 μm. These measured times are used to generate two time-delay histograms for each counter, recorded over both short and long timescales. The short delay histogram has 1023 time bins, each with a width of $t_s = 0.0021701$ ms. The long delay histogram has 1024 bins with a nominal width of $t_l = 64t_s = 0.1389$ ms. Beyond 1024 of these longer bins, corresponding to $t_o = 2^{16}t_s \approx 142$ ms, the time delay overflows, and a count is recorded in the overflow bin. Histograms of these delay times, collected and recorded for each hour, were used to compute the leader fraction as summarized in the following section.

Throughout the observation period, some data gaps occurred, particularly at Changvan, due to power outages and electronic issues. These gaps were excluded when analyzing correlations between the two stations to ensure that the data comparison was accurate and unaffected by missing records. Count rate data were corrected for atmospheric pressure and precipitable water vapor. Data cleaning, reduction, and handling missing data are discussed in detail below.

2.4. Leader Fraction Analysis

The leader fraction serves as a proxy for the spectral index of cosmic rays (P. Muangha et al. 2024). A higher leader fraction indicates a softer cosmic-ray spectrum with more low-energy cosmic rays, while a lower leader fraction suggests a harder spectrum dominated by high-energy cosmic rays. Details of its definition, calculation, and application have been extensively discussed in the literature (D. Ruffolo et al. 2016; C. Banglieng et al. 2020), so we only briefly summarize them here.

In essence, the leader fraction is a measure of the number of neutrons detected without a temporally associated preceding detection in the same counter. It is calculated from the time-delay histograms by fitting an exponential decay to the long time-delay portion of the histogram, which represents unrelated neutron events classified as "leaders." Then the leader fraction is the ratio of leader counts (integrated counts from the exponential fit) to total counts.

Specifically, the leader fraction (L) is calculated following the technique suggested by C. Banglieng et al. (2020) using the equation (P. Yakum et al. 2021)

$$L = \frac{\int_{t_d}^{\infty} A_0 e^{-\alpha t} dt}{\int_{t_d}^{t_o} N(t) dt + \int_{t_o}^{\infty} A_0 e^{-\alpha t} dt}, \quad (1)$$

where A_0 is the initial amplitude of the exponential decay, α is the decay constant describing the rate at which the number of detected neutrons decreases with delay time, and $N(t)$ is the number of neutrons detected at time t in the histogram. The parameter t_d denotes the dead time of the detector, the minimum interval after a detection during which no other events can be recorded. The maximum time limit of the histogram is denoted by t_o; any counts beyond this time result in an overflow, which is recorded in a separate bin. At PSNM the dead time ranges from 72 to 83 μm for various detectors, whereas for Changvan the range is 73–81 μm. For a discrete histogram, Equation (1) becomes

$$L = \frac{(A_0/\alpha)e^{-\alpha t_d}}{\Sigma_{t=t_d}^{t_o} N_t + (A_0/\alpha)e^{-\alpha t_o}}, \quad (2)$$

where N_t is the number of neutrons in the time bin t. Finally, an absolute normalization has been applied for consistency with the values reported by C. Banglieng et al. (2020).

3. Data Cleaning and Correction

The count rates and leader fractions extracted from time-delay histograms are influenced by environmental factors. After data cleaning, corrections for atmospheric pressure and precipitable water vapor are particularly important.

3.1. Data Cleaning

For the PSNM, we use the average count rate from the 18 counter tubes, denoted C_{PSNM}. Outliers are removed by excluding data points that deviate more than $\pm 3\sigma$ from the mean of a Gaussian distribution. This method is also applied to the fitting parameters A_0 and α from the time-delay histograms to refine the hourly leader fraction (L_i) for each tube. The average leader fraction across all tubes is denoted as L_{PSNM}. Between 2021 July 29 and 2021 December 24, six of the tubes operated in a test mode. During this interval, data from affected tubes were ignored. Whenever C or L data were excluded for specific tubes, the averages were rescaled using the data from the remaining tubes.

For the Changvan, the count rates of the three detector tubes are denoted as C_1, C_2, and C_3 and the leader fractions L_1, L_2, and L_3. The hourly average tube ratios C_1/C_2, C_2/C_3, and C_3/C_1 were calculated, with outliers identified as deviations beyond $\pm 3\sigma$ for C_3/C_1 and $\pm 2\sigma$ for C_1/C_2 and C_2/C_3.

Table 2
Barometric Pressure (β) and Precipitable Water Vapor (a) Corrections for the Count Rate C and Leader Fraction L at both PSNM and Changvan

	PSNM		Changvan	
	C	L	C	L
β (% mmHg^{-1})	0.854	−0.00259	Le: 0.854 ± 0.012 Un: 0.786 ± 0.012	Le: −0.016 ± 0.006 Un: −0.011 ± 0.009
a (mm^{-1})	$(10.81 \pm 2.41) \times 10^{-5}$	End: 3.22×10^{-5} Mid: 2.41×10^{-5}	Le: $(8.11 \pm 0.46) \times 10^{-5}$ Un: $(10.84 \pm 0.52) \times 10^{-5}$	Le: $(3.65 \pm 0.72) \times 10^{-5}$ Un: $(2.50 \pm 1.11) \times 10^{-5}$

Note. The reference pressure is taken as 563 mmHg at PSNM and 729.9 mmHg at Changvan. The reference PWV values, chosen based on typical dry season (January) conditions, are 7.2 mm at PSNM and 36.9 mm at Changvan. The abbreviations "End" and "Mid" refer to the end and middle tubes, while "Le" and "Un" denote leaded and unleaded detectors, respectively.

In all cases, small gaps resulting from the cleaning process were filled by normalizing the count rate of the unaffected detectors. Cosmic-ray spectra are significantly and briefly affected during Forbush decrease events, but for this study we wish to focus on more persistent changes. Therefore, data from the obvious Forbush decreases on 2021 November 3–5, 2022 May 19–20, 2022 May 21–22, 2023 February 24–25, 2023 February 27, and 2023 March 23 were excluded.

3.2. Atmospheric Pressure Correction

Neutron count rates and leader fractions are strongly anticorrelated with atmospheric pressure. Higher barometric pressure results from an increase in the total mass of the atmosphere (per unit area) above the detector, leading to greater absorption of cosmic rays and reduced neutron count rates. The leader fraction is also affected by atmospheric pressure but in a different way. To account for this effect, pressure corrections are applied to the data using the following formulas:

$$C_p(t) = C_0(t)\exp\left[\beta_C(p(t) - p_{\rm ref})\right], \quad (3)$$

$$L_p(t) = L_0(t)\exp\left[\beta_L(p(t) - p_{\rm ref})\right], \quad (4)$$

where $C_0(t)$ and $L_0(t)$ are the uncorrected neutron count rate and leader fraction at time t, respectively. $p(t)$ is the barometric pressure measured at the detector at time t, while $p_{\rm ref}$ is a reference pressure, which differs for each station: 563 mmHg for PSNM and 729.9 mmHg for Changvan. The barometric pressure coefficients β_C and β_L are expressed in percent mmHg^{-1}. The numerical values of these coefficients (summarized in Table 2) for PSNM were taken from C. Banglieng et al. (2020), whereas for Changvan, they were determined using the standard method.

3.3. Precipitable Water Vapor Correction

Although the dominant atmospheric influence comes from the total mass above the detector, the composition and distribution of the mass also influence the response. In particular, precipitable water vapor (PWV), the total amount of water vapor contained in a vertical column of the atmosphere, slows down neutrons. As PWV fluctuates with seasonal and local weather conditions, correcting for its effects is crucial for ensuring accurate neutron count rate and leader fraction measurements. We calculate PWV using data from the Global Data Assimilation System (GDAS), and we find it necessary to first smooth the time series of PWV with a triangular filter over ±5 days. The reason why such smoothing is necessary may be the bilinear interpolation in latitude and longitude from the GDAS data on 1° grid points, leading to temporal uncertainty (C. Banglieng et al. 2020). For PSNM data, we use parameters directly from C. Banglieng et al. (2020), while for Changvan data, we determine parameters following the method described in that paper.

The general formulas used for the correction are

$$C_{pw}(t) = C_p(t)\frac{1 - a_C \quad \mathrm{PWV_{ref}}}{[1 - a_C \quad \mathrm{PWV}(t)]}, \quad (5)$$

$$L_{pw}(t) = L_p(t)\frac{1 - a_L \quad \mathrm{PWV_{ref}}}{[1 - a_L \quad \mathrm{PWV}(t)]}, \quad (6)$$

where $C_{pw}(t)$ and $L_{pw}(t)$ are the neutron count rate and leader fraction corrected for both pressure and PWV, while $C_p(t)$ and $L_p(t)$ are the respective quantities corrected only for pressure. Here, a_C and a_L are the negative slopes divided by the intercepts of the linear relationships between the data and PWV. The reference PWV value, $\mathrm{PWV_{ref}}$, differs for each station: 7.2 mm for PSNM and 36.9 mm for Changvan, based on typical dry season (January) conditions. The numerical values of the coefficients are entered in Table 2.

3.4. Corrected Data

Data corrected for pressure and PWV are shown in Figure 2. No clear correlation or anticorrelation between the corrected count rate or leader fraction and either pressure or PWV is visible for either station. We therefore treat the remaining variations in C and L as due to cosmic-ray spectral changes rather than atmospheric effects.

4. Spectral Variations

4.1. Overview of Observations

As used in this paper, the term "spectral variation" refers to characterizing variations in the dependence of the cosmic-ray flux on rigidity, in ways that are more subtle than tracking an integral cosmic-ray flux. Direct measurements by spacecraft are often not publicly available or may have limitations, e.g., in terms of statistics at high rigidity. Comparing data from neutron monitors at different geomagnetic cutoff rigidities, ranging from near zero in polar regions (where an atmospheric cutoff at ∼1 GV becomes dominant) to ∼17 GV in parts of Southeast Asia, is often employed to measure these variations over yearly timescales. However, this technique is not effective for studies of spectral variation at rigidities near and above the highest geomagnetic cutoff on Earth, or over shorter timescales (D. Ruffolo et al. 2016). For such studies, it is important to develop techniques that exploit inherent properties of neutron

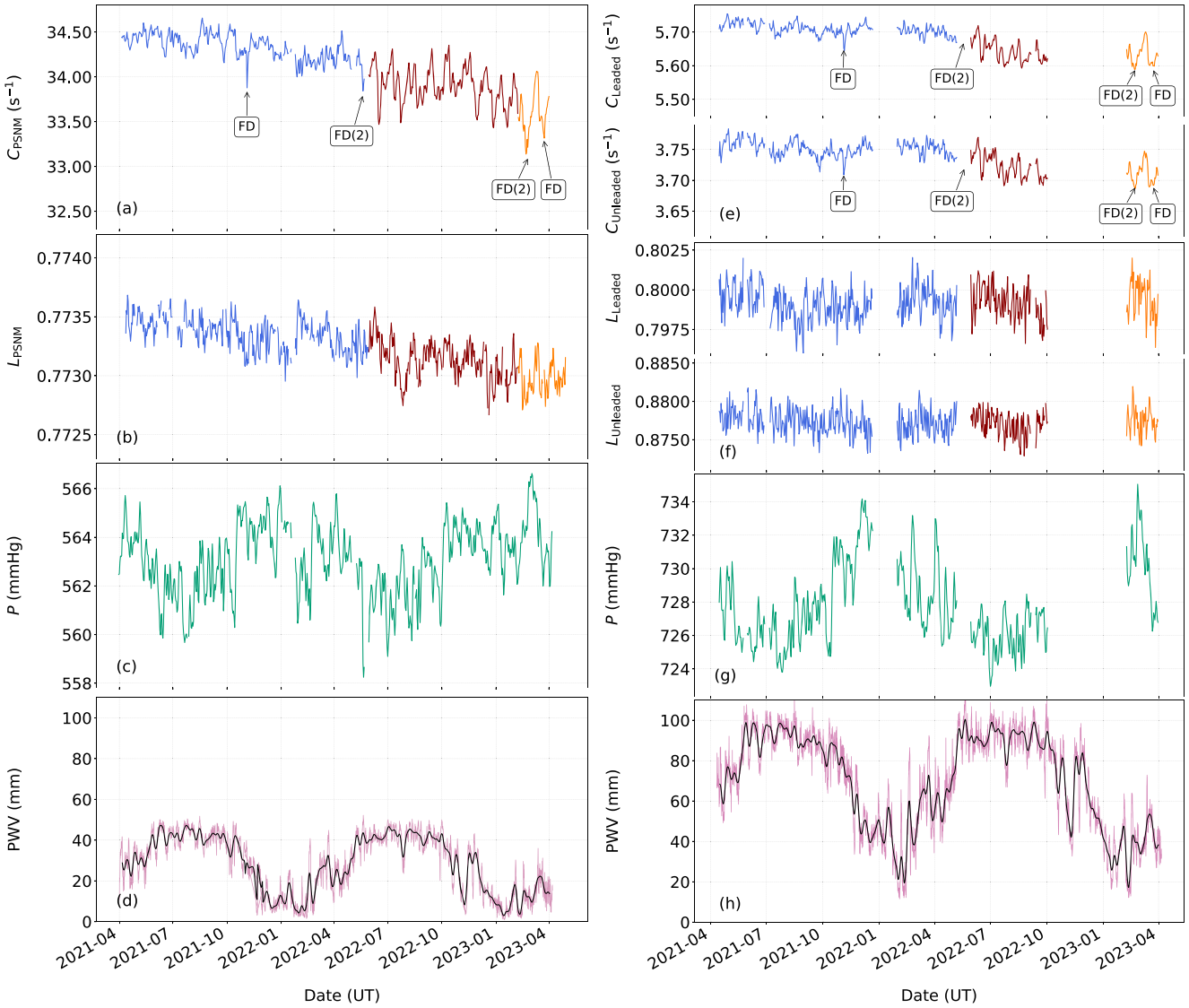

Figure 2. Daily averaged data from neutron detectors at PSNM (left) and Changvan (right), collected between 2021 April and 2023 April. The top panels ((a) and (e)) give the count rate per tube (C). Panels (b) and (f) show the leader fraction (L). Panels (c) and (g) show atmospheric pressure measured at the detector (p, in mmHg), while panels (d) and (h) show the precipitable water vapor (PWV, in millimeters) levels derived from the GDAS atmospheric database. The magenta line shows the unsmoothed data, while the black line represents the data smoothed using a triangular filter applied over a $\pm$5 day interval. Data gaps are due to power outages and electronic issues. Colors in panels (a), (b), (e), and (f) indicate the three time intervals considered in detail. The overall decrease in C and L is associated with solar modulation, i.e., the effect of increasing solar activity during this time period. Selected Forbush decreases are marked with "FD" labels. The number "2" in parentheses indicates two closely spaced decreases.

monitors (or other ground-based detectors) that are sensitive to the energy spectrum of the incident cosmic rays.

P. Muangha et al. (2024) have recently documented a close relationship between the leader fraction at the South Pole neutron monitor, measured since 2015 March, and the differential spectral index over a specific rigidity range as determined from daily proton spectra measured by the space-borne AMS-02 instrument, which have been made public up until 2019 October. Previous work documented that the leader fraction obtained during latitude surveys (P. S. Mangeard et al. 2016b; P. Yakum et al. 2023) indeed responded to the difference in the rigidities of cosmic rays at varying magnetic latitudes, i.e., at varying geomagnetic cutoff rigidities. In the present work, we explore a variety of techniques that are available when using the Changvan and PSNM together at high cutoff rigidity, including the leader fractions from PSNM, Changvan leaded tubes, and the Changvan unleaded tube, as well as the ratios between count rates at different altitudes and between count rates in the leaded versus unleaded counters within the Changvan. The Changvan and PSNM operated in close proximity during the time period of 2021 April to 2023 April, for which AMS-02 proton spectra have not been made public, so we compare between the results of these various techniques to verify their correlations and infer that any and all of them can serve to indicate cosmic-ray spectral variations.

The overall decrease in count rates (C) during this time period, as seen in Figures 2(a) and (e), is a well-known effect of solar modulation, that is, the inverse relationship between solar activity, e.g., as indicated by the sunspot number, and the GCR flux. This period was in the rising phase of the $\sim$11 yr sunspot cycle, so cosmic-ray flux and neutron monitor count rates were decreasing. Another well-known relationship is that solar

modulation and also temporary Forbush decreases due to solar storms have a stronger effect at lower rigidity, so when the flux decreases, the GCR spectrum flattens and the spectral index also decreases. Therefore the leader fraction (L), a measure of the spectral index, basically decreases together with C (C. Banglieng et al. 2020; P. Muangha et al. 2024). Later in this work we will show that the ratios between count rates at different altitudes, as well as the ratio of count rates in the leaded-to-unleaded tubes of the Changvan, vary in the same sense, and therefore also serve as indicators of the spectral index.

In further analysis, we explore the relationships among six parameters (the three count rates and three leader fractions). We consider these relationships separately for three distinct time intervals shown as different colors in panels (a), (b), (e), and (f) of Figure 2. These colors are used consistently in the following figures. Two large Forbush decreases (which occurred during a data gap) form the boundary between an initial period of relatively higher flux with less structure (blue) and a period with overall lower flux with sharp, quasiperiodic structure. Our subsequent analysis suggested the division of the latter period as indicated by the red and orange segments.

Figure 3 shows scatter plots of the 15 possible combinations of parameters, with colors distinguishing time intervals. In essence, these are the elements of a covariance matrix, but the choice of horizontal axis and arrangement of the panels was subjective in an attempt to arrange them in useful order. Each panel shows a colored least-squares fit line to the points of that color, while the black line indicates a fit to all points; parameters of the fits are given in Table 3. All the fits are statistically well defined for the given distribution, but in some cases the slope does not correspond to a real trend in the data. In particular, leader fraction measurements by the Changvan are subject to substantial statistical scatter. Therefore we also show the correlation coefficient for each distribution in the table. In the following discussion, we refer to individual plots by row and column. Thus the upper left panel is "P11" while the bottom right panel is "P53."

4.2. Count Rates

Almost all panels in Figure 3 exhibit what we term spectral variation among intervals. The exception is P53, where statistical variations obscure any possible variation. Note the difference in the range of values plotted for $L_{\rm Leaded}$ in P53 compared to $L_{\rm PSNM}$ in the adjacent panel P52. The better statistics at PSNM resolve differences that would be invisible in P53. There is of course always spectral variation associated with modulation—lower rigidity particles are systematically modulated more heavily than higher rigidity particles, so any change in modulation level typically also occurs with a change in the hardness of the spectrum. Such changes result in systematically related variation of the two parameters, described by the straight line relationships. On the other hand, the color groups of points show differences that are not simply extensions of this relationship.

Average count rates were used to define the blue and red/orange intervals, so it is not surprising that they are separated in panels directly referring to count rates. However, the nature of the separation might be considered interesting. Simple count rate correlations are shown in the top row of Figure 3. In P11, which compares leaded monitors at two different altitudes, the distributions have different slopes. Although the red and blue distributions overlap, the red points are not simply a continuation of the trend of the blue points and vice versa. The orange points form a completely separate distribution. These reflect what we would call a difference in spectral shape. The unleaded monitor behaves differently when compared to either of the leaded monitors. Both altitude and structure are responding to spectral changes but in different ways.

4.3. Leader Fraction and Count Rate

The leader fraction measured at PSNM or the South Pole is a reliable proxy for tracking spectral variations in cosmic rays (D. Ruffolo et al. 2016; C. Banglieng et al. 2020; P. Muangha et al. 2024). A lower leader fraction (for an NM64) indicates a harder cosmic-ray spectrum, while a higher leader fraction suggests a softer spectrum with a greater proportion of lower-energy particles. Hence there are times when the leader fraction can be well correlated with count rate changes, but that is not necessarily always the case. Figure 3 exhibits both types of behavior. In P21, with only PSNM data, there is a much stronger variation of leader fraction with count rate in the red/orange points compared to the blue, but both distributions are quite distinct. The other panels comparing count rates and/or $L_{\rm PSNM}$ (P11, P12, P13, P31, and P41) exhibit similar but slightly different behavior. On the other hand, the panels involving $L_{\rm Leaded}$ or $L_{\rm Unleaded}$ exhibit differences between colored fit lines that are dominated by the scatter in those data.

We observe a structural difference of the unleaded detector, which in a rough sense reverses the origin of the leaders and the followers. A "leader" is the first count in a multiplicity cluster arising from an interaction in the lead. The leader fraction in essence measures the number of leaders without followers. Most of the counts in the unleaded tube result from neutrons generated in the lead of the adjacent tubes. These would ordinarily be followers in one of the other counters, but some are now leaders, and a different pattern in the capture is not surprising. Future work could examine this pattern using Monte Carlo simulations.

4.4. Leader Fraction

The bottom row of Figure 3 compares the different leader fraction measurements. For PSNM there is a separation on average among the color groups, but there is a significant overlap in the distributions and only a modest trend within each distribution. The behavior of the leader fraction is not greatly affected by altitude difference.

5. Discussion and Summary

All the parameters considered react in different ways that can be characterized by comparing the parameter change to the total counting rate of the monitor. Over long intervals, each parameter follows the counting rate with significant scatter but a definite linear trend. These long-term relationships change in character from one time interval to another. In our study we have identified three such intervals, which happen to have significantly different count rates.

5.1. Principal Component Analysis

To explore the various relationships further, we performed a principal component analysis (PCA) of the data, with the result shown in Figure 4. Only the first two components, given

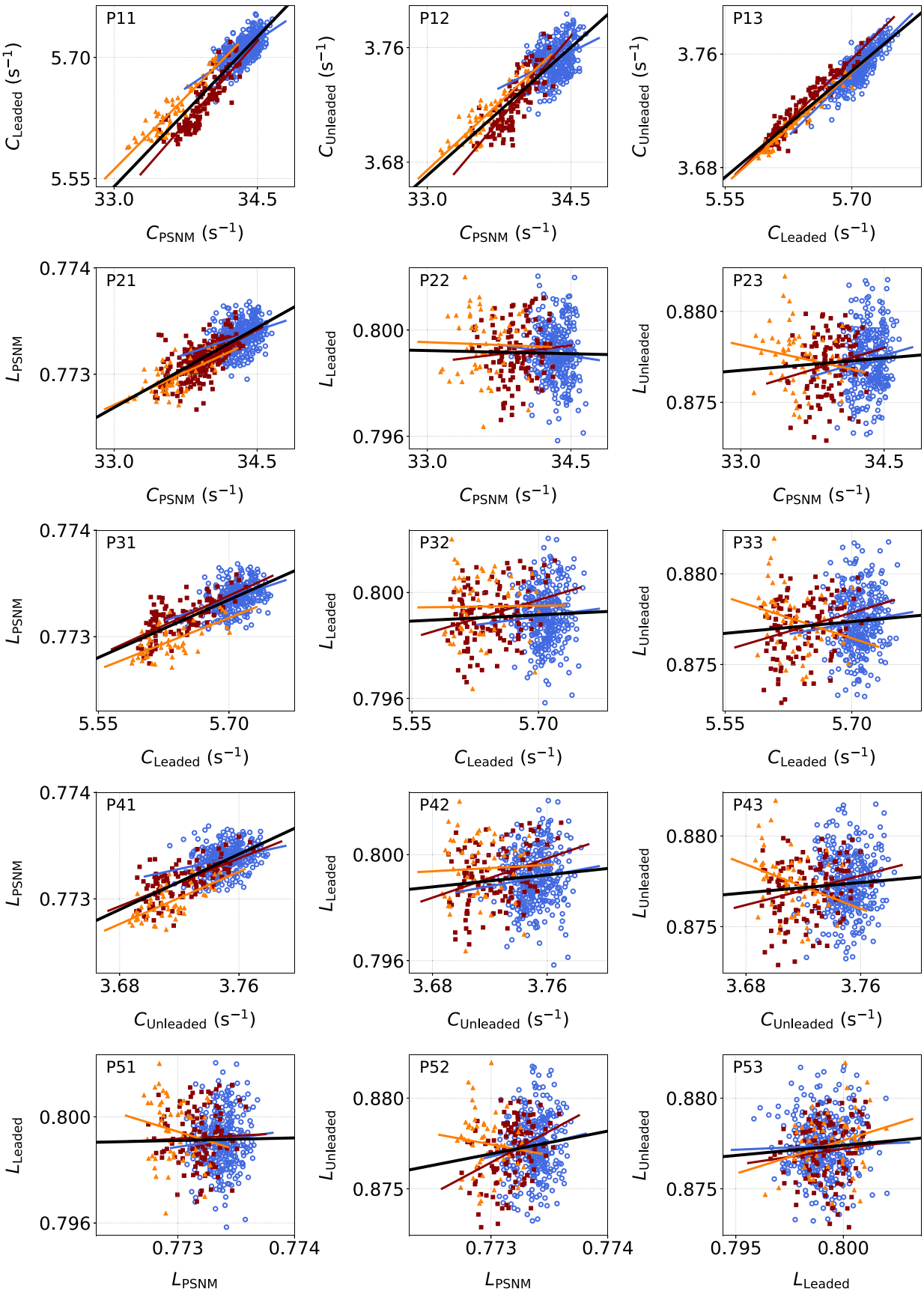

Figure 3. Daily averaged values of the six parameters covered in this study presented as all possible scatter plots. Colors of points and fit lines distinguish the time intervals; the black lines indicate fits to all data. Parameters of the fit lines are shown in Table 3.

Table 3
The Coefficients of Linear Fitting for the Blue, Red, and Orange Groups from Figure 3 as Well as Overall Fitting to All Data

Panel Index	Blue Fitting Parameters			Red Fitting Parameters			Orange Fitting Parameters			Overall Fitting Parameters		
	Slope	Intercept	r^2	Slope	Intercept	r^2	Slope	Intercept	r^2	Slope	Intercept	r^2
P11	0.079 ± 0.005	2.986 ± 0.184	0.40	0.135 ± 0.008	1.050 ± 0.256	0.73	0.120 ± 0.008	1.608 ± 0.264	0.82	0.124 ± 0.003	1.450 ± 0.088	0.83
P12	0.034 ± 0.005	2.599 ± 0.159	0.14	0.079 ± 0.005	1.041 ± 0.182	0.65	0.062 ± 0.005	1.614 ± 0.165	0.76	0.060 ± 0.002	1.702 ± 0.063	0.69
P13	0.586 ± 0.022	0.406 ± 0.124	0.68	0.589 ± 0.018	0.399 ± 0.099	0.91	0.524 ± 0.019	0.761 ± 0.109	0.94	0.497 ± 0.008	0.915 ± 0.046	0.89
P21	0.000 ± 0.000	0.763 ± 0.002	0.10	0.000 ± 0.000	0.757 ± 0.001	0.37	0.000 ± 0.000	0.759 ± 0.002	0.39	0.001 ± 0.000	0.756 ± 0.001	0.56
P22	−0.001 ± 0.000	0.818 ± 0.014	0.01	0.000 ± 0.001	0.784 ± 0.017	0.01	−0.000 ± 0.001	0.804 ± 0.025	0.00	−0.000 ± 0.000	0.802 ± 0.006	0.00
P23	0.002 ± 0.001	0.825 ± 0.023	0.02	0.002 ± 0.001	0.823 ± 0.026	0.04	−0.001 ± 0.001	0.916 ± 0.034	0.03	0.000 ± 0.000	0.862 ± 0.009	0.01
P31	0.003 ± 0.000	0.758 ± 0.002	0.13	0.004 ± 0.000	0.752 ± 0.002	0.46	0.003 ± 0.001	0.755 ± 0.003	0.41	0.004 ± 0.000	0.753 ± 0.001	0.56
P32	0.004 ± 0.003	0.775 ± 0.018	0.00	0.010 ± 0.003	0.746 ± 0.017	0.08	0.000 ± 0.006	0.797 ± 0.031	0.00	0.002 ± 0.001	0.790 ± 0.007	0.00
P33	0.008 ± 0.005	0.830 ± 0.030	0.01	0.014 ± 0.005	0.799 ± 0.026	0.07	−0.015 ± 0.007	0.963 ± 0.042	0.08	0.004 ± 0.002	0.853 ± 0.011	0.01
P41	0.003 ± 0.001	0.762 ± 0.002	0.08	0.006 ± 0.001	0.752 ± 0.002	0.39	0.006 ± 0.001	0.750 ± 0.004	0.43	0.007 ± 0.000	0.749 ± 0.001	0.50
P42	0.010 ± 0.005	0.762 ± 0.017	0.01	0.019 ± 0.005	0.730 ± 0.018	0.11	0.003 ± 0.010	0.788 ± 0.038	0.00	0.006 ± 0.002	0.778 ± 0.009	0.01
P43	0.007 ± 0.007	0.852 ± 0.027	0.00	0.020 ± 0.008	0.802 ± 0.028	0.06	−0.031 ± 0.014	0.991 ± 0.050	0.09	0.007 ± 0.004	0.851 ± 0.014	0.01
P51	0.656 ± 0.457	0.292 ± 0.354	0.01	0.232 ± 0.570	0.620 ± 0.441	0.00	−1.355 ± 1.113	1.847 ± 0.860	0.03	0.096 ± 0.260	0.725 ± 0.201	0.00
P52	1.557 ± 0.729	−0.327 ± 0.564	0.01	3.442 ± 0.838	−1.784 ± 0.648	0.13	−1.193 ± 1.576	1.800 ± 1.218	0.01	1.255 ± 0.407	−0.094 ± 0.315	0.02
P53	0.050 ± 0.088	0.838 ± 0.070	0.00	0.176 ± 0.140s	0.736 ± 0.112	0.01	0.367 ± 0.190	0.584 ± 0.152	0.07	0.111 ± 0.072	0.789 ± 0.057	0.01

Note. Each panel index (P11–P53) corresponds to a linear fit applied separately to each group, providing slope, intercept, and coefficient of determination (r^2) values. The r^2 value represents the goodness of fit, indicating how well the linear model explains the variance in the data. Higher r^2 values suggest a stronger linear relationship between the variables for the respective group. Uncertainties in the slope and intercept indicate standard errors.

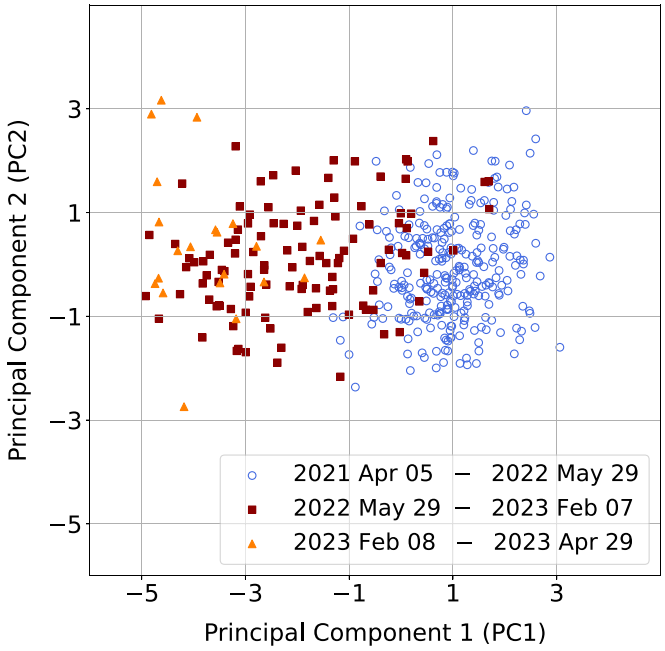

Figure 4. Principal component analysis (PCA) of the data shown in Figure 3. The plot displays the distribution of data along the first two principal components in Equations (7) and (8), which capture the majority of the variance in the data set.

explicitly as Equations (7) and (8), are significant.

$$\begin{aligned}\mathrm{PC1} = {} & 0.503 \cdot C_{\mathrm{PSNM}} + 0.526 \cdot C_{\mathrm{Leaded}} + 0.506 \cdot C_{\mathrm{Unleaded}} \\ & + 0.453 \cdot L_{\mathrm{PSNM}} + 0.018 \cdot L_{\mathrm{Leaded}} \\ & + 0.092 \cdot L_{\mathrm{Unleaded}}\end{aligned} \tag{7}$$

$$\begin{aligned}\mathrm{PC2} = {} & -0.124 \cdot C_{\mathrm{PSNM}} - 0.042 \cdot C_{\mathrm{Leaded}} + 0.000 \cdot C_{\mathrm{Unleaded}} \\ & + 0.030 \cdot L_{\mathrm{PSNM}} + 0.771 \cdot L_{\mathrm{Leaded}} \\ & + 0.622 \cdot L_{\mathrm{Unleaded}}\end{aligned} \tag{8}$$

Plotted against each other, the components show a rather complete separation of the red/orange and blue intervals along the PC1 axis with a somewhat different relation between the two components in the different groups. The orange and red groups are split primarily along the PC2 axis. From the analysis coefficients it is immediately clear that the count rate has a major influence on PC1, leaving the question of the real difference between the red and blue intervals open. We therefore conducted an analysis using only count rate ratios rather than the count rates themselves. There are several ways to take ratios and combine them, but every case we considered resulted in some separation of the red/orange and blue points.

We show one example in Figure 5. Again, only the first two components, given explicitly as Equations (9) and (10), are significant. Considering the count rate itself is not necessary to achieve a clear separation of the red and blue intervals, but the separation of the orange and red is less clear.

$$\begin{aligned}\mathrm{PC1} = {} & 0.613 \cdot \frac{C_{\mathrm{Leaded}}}{C_{\mathrm{Unleaded}}} + 0.592 \cdot \frac{C_{\mathrm{PSNM}}}{C_{\mathrm{Unleaded}}} \\ & + 0.490 \cdot L_{\mathrm{PSNM}} - 0.132 \cdot L_{\mathrm{Leaded}} \\ & + 0.132 \cdot L_{\mathrm{Unleaded}}\end{aligned} \tag{9}$$

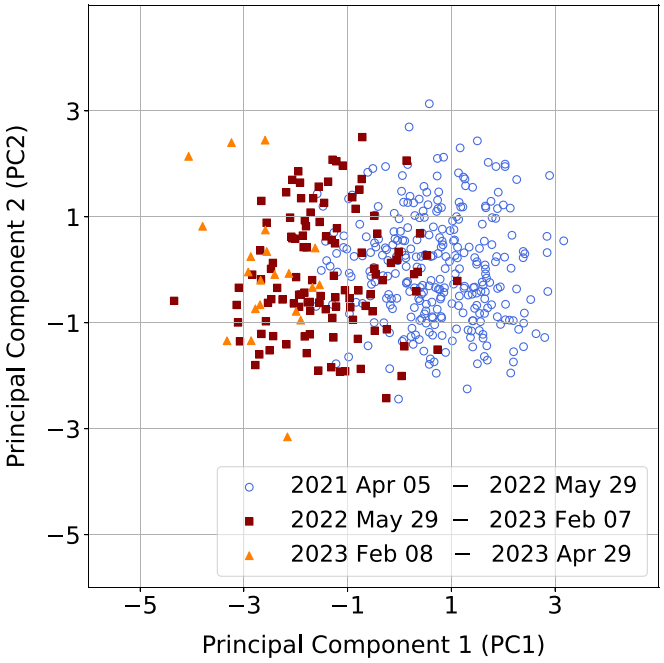

Figure 5. Principal component analysis of the data shown in Figure 3 but for count rate ratios only. The plot displays the separation between the blue and red groups along the first two principal components in Equations (9) and (10).

$$\begin{aligned}\mathrm{PC2} = {} & -0.038 \cdot \frac{C_{\mathrm{Leaded}}}{C_{\mathrm{Unleaded}}} - 0.174 \cdot \frac{C_{\mathrm{PSNM}}}{C_{\mathrm{Unleaded}}} \\ & + 0.270 \cdot L_{\mathrm{PSNM}} + 0.693 \cdot L_{\mathrm{Leaded}} \\ & + 0.644 \cdot L_{\mathrm{Unleaded}}\end{aligned} \tag{10}$$

5.2. Discussion

Guided by the PCA, we constructed a relation between two parameters—the PSNM leader fraction and the leaded/unleaded count rate ratio—that best characterized the results. In this representation, shown in the left panel of Figure 6, the red and blue points appear to be at separate ends of a continuum rather than separate distributions, whereas the orange points are completely distinct. To characterize the relationships better, we performed some simple statistical tests. A linear mixed model analysis shows that the slope of the relationship is indistinguishable for all three groups. However, an analysis of variance, or ANOVA, which is a statistical method for comparing means among multiple groups, shows that the three groups are very distinct. The right panel of Figure 6 provides additional insights into temporal variations as well as the influence of altitude differences on the observed count rate ratios.

5.3. Summary

In summary, we have explored the use of a novel semileaded neutron monitor, the Changvan, to track short-term spectral variations of cosmic rays. While designed to perform shipborne latitude surveys, the Changvan can also perform useful measurements at a fixed location. In addition to the usual count rate measurements to track the GCR flux, the count rate ratio between the leaded and unleaded counters provides an innovative measure of the GCR spectral index. The leader fraction at any altitude also responds to spectral changes, while parameter variations are related in different ways such that no parameter is completely predicted by any combination of the

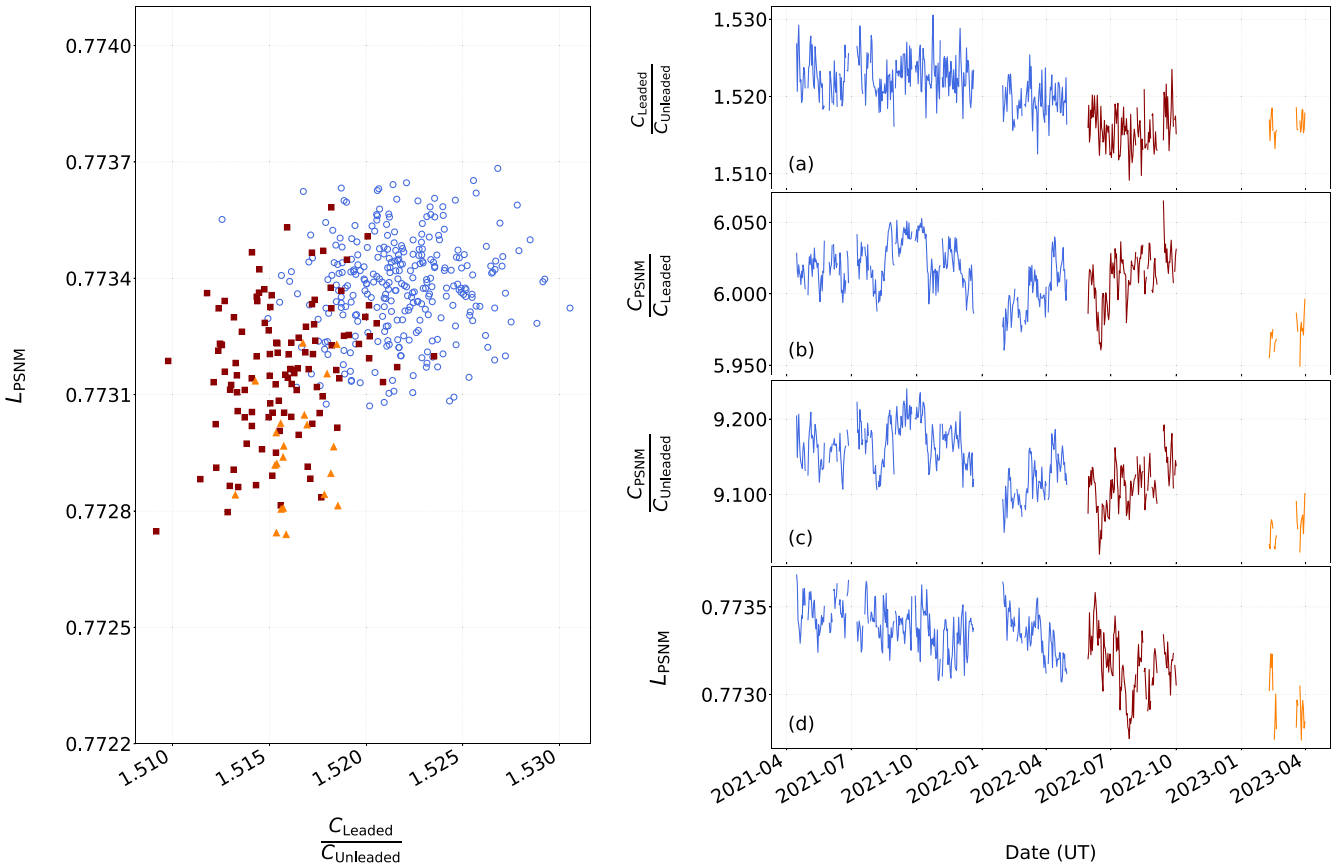

Figure 6. (Left) Combination of parameters showing the transition between two of the time periods studied (red and blue) as part of a continuum of variations. The pattern is slightly different for the third interval (orange). (Right) Time series plots of (a) the leaded-to-unleaded count rate ratio $C_{\rm Leaded}/C_{\rm Unleaded}$, (b) the altitude-dependent count rate ratio $C_{\rm PSNM}/C_{\rm Leaded}$, (c) another altitude-dependent count rate ratio $C_{\rm PSNM}/C_{\rm Unleaded}$, and (d) the leader fraction $L_{\rm PSNM}$ (previously demonstrated to measure the spectral index), showing the temporal evolution of these parameters across the total time period. Overall, they all provide consistent indicators of the cosmic-ray spectral index as it varies according to solar modulation.

others. Furthermore, by choosing a fixed location near the larger PSNM but at a very different altitude, we can also use the count rate ratio between the two monitors to indicate the spectral variations. This altitude technique has previously been used at low cutoff rigidity to estimate the spectral index of solar energetic particles during ground level enhancement events, which are sudden increases in cosmic-ray intensity observed by ground-based detectors during major solar eruptions, and now we apply it to study GCRs at high cutoff rigidity. A particular significance of performing these measurements at high cutoff rigidity is that we can learn about the GCR spectrum over a rigidity range beyond the world's highest cutoff, i.e., beyond the reach of latitude surveys or count rate comparisons from the same type of detector at different cutoffs. With modeling and comparison to direct spectral determinations, the prospects are good that GCR spectral variations can be even better characterized from the neutron monitor data.

Acknowledgments

This research was made possible through the support of Chiang Mai University, which provided an RA scholarship and partial funding under the CMU Proactive Researcher grant (grant No. 905/2567). Additional funding was received from the National Science and Technology Development Agency (NSTDA) and the National Research Council of Thailand (NRCT) through the High-Potential Research Team Grant Program (N42A650868), as well as from the NSRF via the Program Management Unit for Human Resources and Institutional Development, Research and Innovation (B39G670013, B41G680027). This project was partially funded by the National Research Council of Thailand (NRCT) under grant No. N42A661044. We sincerely thank the Information Technology Service Center (ITSC) at Chiang Mai University for the provision of an on-demand server, which was crucial for this work. We extend our special thanks to Mr. Ekkarach Somboon, a dedicated support staff member at Chiang Mai University, whose invaluable contributions were instrumental in the construction of the Changvan neutron monitor and the establishment of a comprehensive data repository. Our appreciation also goes to the Northern Science Park (Chiang Mai) for generously providing laboratory space, which significantly advanced our research team's progress.

ORCID iDs

S. Khamphakdee https://orcid.org/0009-0008-8182-1180
W. Nuntiyakul https://orcid.org/0000-0002-1664-5845
C. Banglieng https://orcid.org/0000-0002-4862-2015
A. Seripienlert https://orcid.org/0000-0002-3764-8949
P. Yakum https://orcid.org/0009-0000-7520-3038
A. Sáiz https://orcid.org/0000-0001-7771-4341
D. Ruffolo https://orcid.org/0000-0003-3414-9666
P. Evenson https://orcid.org/0000-0001-7929-810X
K. Munakata https://orcid.org/0000-0002-2131-4100
S. Komonjinda https://orcid.org/0000-0001-7987-017X

References

Aleksanyan, T. M., Bednazhevsky, V. M., Blokh, Y. L., Dorman, L. I., & Starkov, F. A. 1979, ICRC (Tokyo), 16, 315
Banglieng, C., Janthaloet, H., Ruffolo, D., et al. 2020, ApJ, 890, 21
Belov, A. 2000, SSRv, 93, 79
Bieber, J. W., Clem, J., Evenson, P., et al. 2013, ApJ, 771, 92
Bieber, J. W., Clem, J. M., Duldig, M. L., et al. 2004, JGRA, 109, A12106
Bieber, J. W., Dröge, W., Evenson, P. A., et al. 2002, ApJ, 567, 622
Bieber, J. W., & Evenson, P. 1991, ICRC (Dublin), 22, 129
Kudela, K., Storini, M., Hofer, M. Y., & Belov, A. 2000, SSRv, 93, 153
Lara, A., Borgazzi, A., & Caballero-Lopez, R. 2016, AdSpR, 58, 1441
Lockwood, J. A., Debrunner, H., Flueckiger, E. O., & Ryan, J. M. 2002, SoPh, 208, 113
Mangeard, P.-S., Clem, J., Evenson, P., et al. 2018, ApJ, 858, 43
Mangeard, P. S., Ruffolo, D., Sáiz, A., Madlee, S., & Nutaro, T. 2016a, JGRA, 121, 7435
Mangeard, P. S., Ruffolo, D., Sáiz, A., et al. 2016b, JGRA, 121, 620
Mavromichalaki, H., Papaioannou, A., Plainaki, C., et al. 2011, AdSpR, 47, 2210
Mishev, A., Koldobskiy, S., Kovaltsov, G., Gil, A., & Usoskin, I. 2021, PoS, ICRC2021, 1247
Muangha, P., Ruffolo, D., Sáiz, A., et al. 2024, ApJ, 974, 284
Nuntiyakul, W., Sáiz, A., Ruffolo, D., et al. 2018, JGRA, 123, 7181
Poopakun, K., Nuntiyakul, W., Khamphakdee, S., et al. 2023, ApJ, 958, 80
Potgieter, M. S. 2013, LRSP, 10, 3
Ruffolo, D., Sáiz, A., Mangeard, P. S., et al. 2016, ApJ, 817, 38
Ruffolo, D., Tooprakai, P., Rujiwarodom, M., et al. 2006, ApJ, 639, 1186
Simpson, J. A. 1983, ARNPS, 33, 323
Simpson, J. A. 2000, SSRv, 93, 11
Yakum, P., Jiang, P., Chuanraksasat, P., et al. 2021, JPhCS, 1719, 012006
Yakum, P., Khamphakdee, S., Nuntiyakul, W., et al. 2023, JPhCS, 2653, 012019